Journal of Geophysical Research: Solid Earth

RESEARCH ARTICLE
10.1002/2017JB015162

Key Points:
- A wave propagation code (SPECFEM2D) and a mechanical deformation code (Code_Aster) are combined in a new modeling framework
- Elastic deformation induces time shifts in coda waveforms
- Strain measurements from coda wave interferometry are shown to be possible

Supporting Information:
- Supporting Information S1
- Figure S1
- Figure S2
- Figure S3

Correspondence to:
J. Azzola,
jerome.azzola@unistra.fr

Citation:
Azzola, J., Schmittbuhl, J., Zigone, D., Magnenet, V., & Masson, F. (2018). Direct modeling of the mechanical strain influence on coda wave interferometry. *Journal of Geophysical Research: Solid Earth*, *123*, 3160–3177. https://doi.org/10.1002/2017JB015162

Received 1 NOV 2017
Accepted 23 MAR 2018
Accepted article online 30 MAR 2018
Published online 25 APR 2018

Direct Modeling of the Mechanical Strain Influence on Coda Wave Interferometry

J. Azzola[1], J. Schmittbuhl[1], D. Zigone[1], V. Magnenet[2], and F. Masson[1]

[1]IPGS/EOST, Strasbourg University/CNRS, Strasbourg, France, [2]ICUBE, Strasbourg University/CNRS, Strasbourg, France

Abstract Coda waves interferometry (CWI) aims at tracking small changes in solid materials like rocks where elastic waves are diffusing and so intensively sampling the medium, making the technique more sensitive than those relying on direct wave arrivals. Its application to ambient seismic noise correlation, referred to as ambient noise interferometry, has found a large range of applications over the past years like for reservoir monitoring or regional fault evolution. Physically, the changes in phases observed are typically interpreted as small variations of seismic velocities. However, this interpretation is questionable. The goal of the present work is to show from a direct numerical modeling that deformation signal also exists in CWI measurements which might provide new outcomes for the technique. For this purpose, we model seismic wave propagation within a diffusive medium using a spectral element approach (SPECFEM2D) during an elastic deformation of the medium. The mechanical behavior is obtained from a finite element approach (*Code_Aster*) keeping the mesh grid of the sample constant during the whole procedure to limit numerical artifacts. CWI of the late wave arrivals in the synthetic seismograms is performed using both a stretching technique in the time domain and a frequency cross-correlation method. Both show that CWI is sensitive to the heterogeneity of the elastic deformation field in addition to the isotropic volumetric deformation and independently of nonlinear acoustoelastic effects. Implications for strain monitoring of reservoirs are discussed.

1. Introduction

In seismology, coda waves are associated to the late part of an earthquake seismogram. On the contrary, to direct seismic phases, coda waves result from multiple scattering produced by small-scale heterogeneities in the Earth's crust (Aki, 1969, 1980; Aki & Chouet, 1975) and therefore cannot be studied with classical ray theory. To overcome this limitation, several approaches such as radiative transfer theory (e.g., Margerin et al., 1999, 2016; Wu, 1985) along with mode equipartition (Weaver, 1982) have been used to characterize the diffusive properties of the coda. One of its main characteristic is the stabilization of energy ratios between *S* and *P* waves at large lapse time, which is commonly referred to as equipartition (e.g., Ryzhik et al., 1996; Weaver, 1982, 1990). This property comes directly from radiative transfer theory (Ryzhik et al., 1996; Weaver, 1990) and has also been demonstrated for coda waves both numerically (e.g., Margerin et al., 2000) and on real earthquakes data (e.g., Shapiro et al., 2000). The equipartition of coda waves and their overall diffusive nature (Hennino et al., 2001) makes them highly repeatable and very sensitive to weak changes of the medium (Snieder, 2006) since their paths extensively sample the material through multiple scattering. This sensitivity is the principle of coda wave interferometry (CWI), a technique that estimates slight traveltime perturbations from a direct comparison of waveform changes in the coda before and after a perturbation.

The increasing use of CWI as a highly sensitive monitoring tool has followed the rapid development of Green's function reconstruction either from earthquake coda waves (Campillo & Paul, 2003) or from ambient seismic noise (Roux et al., 2005; Shapiro & Campillo, 2004). This later method, known as ambient noise interferometry, allows the reconstruction of virtual active sources at every passive station by cross-correlating continuous seismic noise records between every pair of stations (see Campillo & Roux, 2015, for a review). Such noise-based applications have recently revolutionized the use of seismic arrays to image the upper crustal structures of the earth (Boué et al., 2014; Lin et al., 2013; Moschetti et al., 2007; Shapiro et al., 2005; Zigone et al., 2015). Since this approach does not rely anymore on any kind of active or passive punctual sources (e.g., earthquakes and blasts), the resolution is entirely governed by the geometry and density of the network, and, since seismic noise is a continuous and pervasive wavefield, it can be applied everywhere and allow monitoring changes in the crust by comparing records at different times. Examples include the monitoring

of fault zones or mud landslides (Mainsant et al., 2012) and could help to forecast volcanic eruptions (Brenguier et al., 2008, 2011; Duputel et al., 2009) for which seismic velocity decreases are highlighted few weeks prior to eruptions. Recently, it has been shown to be relevant for imaging and monitoring the geothermal reservoir in the area of Rittershoffen (northeast of France) where a deep geothermal plant (2,500 m) is installed (Lehujeur et al., 2014). Seismic velocity changes (in case of reservoir applications or at a larger scale for crustal seismic velocity changes) can occur due to several factors such as water saturation related to rainfalls, air pressure, stress, or temperature changes (Lockner et al., 1977; Planès & Larose, 2013; Snieder, 2002).

However, it is generally challenging to interpret these temporal changes observed in records as disruptive events. Indeed, time shifts measured by CWI generally include all the physical sensitivities of diffuse wavefield, including reversible or irreversible phenomena such as wave velocities, anisotropy, temperature gradient, stress changes, or evolving scattering properties. Because of this broad sensitivity, the causal link that exists between time delays observed in the recorded seismograms and the physical processes at play in situ is complex. One faces the same difficulties in laboratory experiments, where multiple effects are generally difficult to distinguish (Snieder, 2006). Because of the complexity of studying the partitioning between the different competing physical processes responsible for time delay in CWI measurements, most seismic interferometry studies make the hypothesis that velocity changes dominate the signals (Yamamura et al., 2003). Such hypothesis is reasonable when considering small velocity and deformation changes with purely volumetric deformation. However, those conditions are not necessarily met in natural environments, which lets the question open on the relative contributions of deformation and velocity changes in CWI delay measurements.

The present work aims at a better understanding of the physical changes deduced from CWI with a focus on the strain influence on interferometry measurements. In order to test the partitioning between the different physical phenomena in question, we combine both elastic deformation and seismic wave propagation modeling, in which parameters and disruptive elements are easily managed. This numerical approach allows subsequently to test the effect of the material deformation independently of intrinsic wave velocity variations related to inelastic deformation (microcracks, plastic deformation, etc.).

The elastic deformation of an idealized diffusive sample is obtained from a finite element approach (*Code_Aster*). We perform a direct numerical modeling of seismic wave propagation within the sample using a spectral element approach (SPECFEM2D) during its deformation. As an illustration, the modeled sample is chosen as an effective medium (70 cylindrical holes as scatters randomly distributed in a homogeneous elastic block) aiming to mechanically and acoustically reproduce a typical reservoir rock like the granite of the deep geothermal site of Soultz-sous-Forêts, France. The same grid mesh of the sample is conserved during the whole procedure to limit numerical artifacts in particular numerical diffusion.

The manuscript is organized as follows: after an introduction, section 2 presents the developed method, the choice of the effective propagation medium, and the optimal distribution of scatters to simulate a granite sample prepared from a Soultz-sous-Forêts borehole core. Section 3 details the tests performed to check the mechanical and acoustic behavior of the medium. In section 4, we present the CWI technique and its application for strain assessment using two methods: a stretching technique in the time domain and a complementary time window cross-correlation method. Section 5 is devoted to the discussion of the results.

2. Materials and Methods

2.1. Numerical Scheme

Figure 1 shows a sketch of the numerical experiment. A mechanical loading δ is applied to an effective medium that simulates a granite block, by imposing a rigid displacement of its upper face. At each step of the loading, an impulsive Ricker wavelet of central frequency f_0 is sent through the medium from a seismic source set on the left side of the sample. The seismogram at the receiver on the opposite (right) face is then numerically computed as the acceleration of the particle motion. It includes the direct wave arrivals and the late coda wave arrivals.

The numerical scheme consists of three steps. At the initiation of the simulation, the block is discretized using a 2-D finite element mesh grid. It is then iteratively deformed using the finite element software *Code_Aster* (open source *Code_Aster*—general FEA software http://www.code-aster.org). More specifically, a rigid displacement δ is imposed at the upper face of the plate and successively increased step by step. The calculation

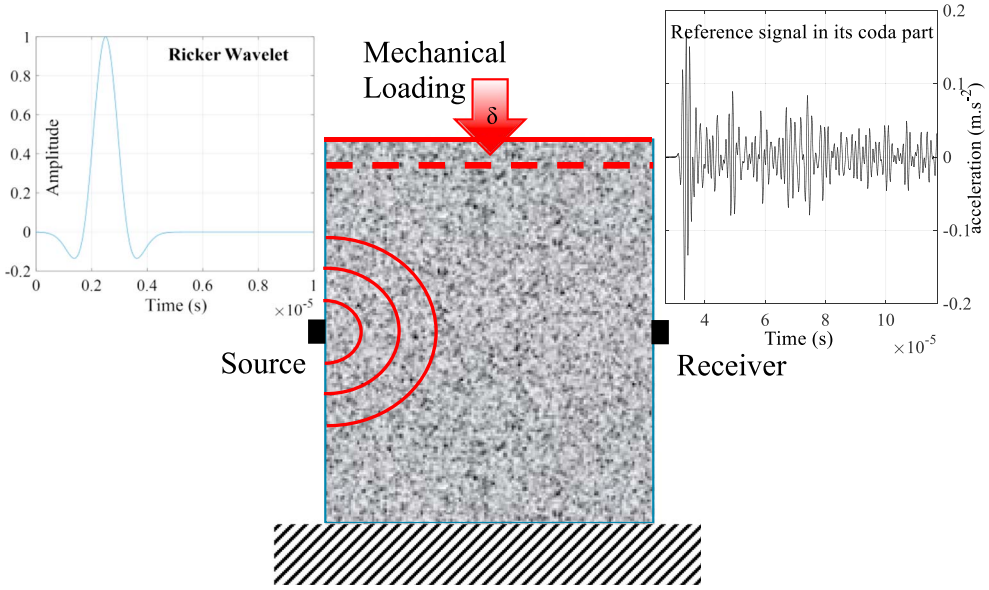

Figure 1. Principle of the numerical experiment: We impose a mechanical loading δ to a rock sample imposing a rigid step-by-step displacement of the upper face. During the loading, a Ricker wavelet (see left insert) is sent in the medium from the source and recorded at the opposite face by the receiver (see right insert).

results in a displacement field at the nodes of each finite element. The current mesh grid is then deformed accordingly and transferred to a second code, SPECFEM2D (a 2-D spectral element code; see Komatitsch & Vilotte, 1998), to simulate the wave propagation in the medium from the emitted source, taking advantage of the high degree of the trigonometric polynomial basis functions of the spectral element method. Importantly, the wave velocities in all elements are kept constant during all the steps. The mesh grid is the only parameter that evolves during the successive simulations. This numerical approach allows subsequently to test the effect of the elastic deformation independently of intrinsic wave velocity variations related to anelastic processes like damage development. It is in this case a real advantage with respect to laboratory experiments where both effects are generally very difficult to distinguish (Snieder, 2006). In the following, the reference seismogram refers to the one recorded when no displacement is imposed, and the perturbed seismogram refers to the one recorded after a given displacement δ. Seismograms are compared sequentially using CWI in order to analyze changes induced by the deformation.

2.2. Sample Description

2.2.1. Effective Medium

Figure 1 explains our method for setting an effective medium to model wave diffusion in a granite sample. We recall that a granite rock is a plutonic rock typically composed of orthoclase feldspar, quartz, plagioclase feldspar, mica, and amphibole in which one can identify millimetric grains. We chose to sketch the complex mineral assembly of the granite that is responsible for wave diffusion, as a discrete set of scatters in a homogeneous elastic material. In our model, scatters consist of circular holes with a radius of 3 mm and behaving as inclusions of grains. The sample is of size 112 mm × 95 mm and includes 70 scatters randomly distributed in space. The objective is to obtain similar wave diffusion properties of our idealized sample compared to experimental samples. Details of the procedure for reproducing experimental properties are given in section 3.3.

2.2.2. Boundary Conditions

For the wave propagation (SPECFEM2D), the top, bottom, right, and left sides of the block are chosen as absorbent boundaries. The absorbent condition is a so-called Stacey boundary condition defined in Stacey (1988) such that the total energy of the system can be neglected once the first *P* and *S* wave are propagated in the medium (Komatitsch & Tromp, 2003). During the mechanical loading (*Code_Aster*), a vertical displacement is imposed at the top of the sample, the bottom being fixed (no horizontal and vertical displacement). Left and right borders are under free boundary conditions; that is, normal stress is set to 0.

2.2.3. Mechanical Parameters

The elastic parameters of the bulk material are taken from triaxial tests conducted on nonaltered granite samples from the GPK-1 well at Soultz-sous-Forêts (Rummel, 1992). The chosen elastic parameters of the medium are respectively for the Young modulus: E = 54 GPa and the Poisson ratio: ν = 0.26. The density is chosen to be ρ = 2,570 kg/m^3. The elastic limit is set to R_e = 150 MPa. The estimated P wave velocity is 5,070 m/s, and the estimated S wave velocity is 2,888 m/s. Holes in our model are assumed to be air filled with elastic parameters (E, ν) values 10^9 times lower than those used for the surrounding elastic medium, so that the holes are also elastically deformed during the loading.

2.2.4. Sample Meshing

The 2-D geometry of the mesh grid is generated using GMSH (http://gmsh.info) which is a GNU General Public License finite element mesh generator that can be used to generate 2-D quadrangle meshes processed both by SPECFEM2D and *Code_Aster*. The 2-D mesh is obtained using a Delaunay algorithm and is optimized for four nodded quadrangle elements. The optimization and recombination are performed using the default Blossom algorithm using a minimum cost perfect matching algorithm to generate fully quadrilateral meshes from triangulations (Remacle et al., 2012). The mesh grid considered in this study includes 235,611 elements of characteristic length l_c = 0.5 mm. This parameter influences the refinement of the mesh grid and corresponds to the characteristic distance between two successive nodes. The validation of the mesh quality is described in the supporting information S1.

The quality of the coupling between the static mechanical deformation (*Code_Aster*) and the dynamic wave propagation (SPECFEM2D) is conditioned by enabling the two codes to treat a common mesh grid at any step of the loading. In GMSH, the geometry of the effective medium is described using a boundary representation defining points, oriented lines, and surfaces. These basic geometric entities can be grouped. Their grouping defines "physical entities" which are specific units of the mesh featuring each material type. Here the circles defining the holes, filled with air, are grouped and define a first physical entity. The geometric entities limiting the surrounding, constituting granite, define a second physical entity. This enables to affect the physical properties specific to each material type to the elements of each physical entity in both SPECFEM2D and *Code_Aster*. A high-quality coupling of these codes relies on the use of the same physical entities and the same meshes in both codes which needs a relevant mesh format conversion from SPECFEM2D (GMSH format) MSH format, Gmsh's native mesh file format to *Code_Aster* ("Modélisation et Échanges de Données" (MED) format). The mechanical plane-strain simulation results in the calculation of the displacement field at each node of the elements. The displacement at each node of the mesh is done by arithmetic means of the displacement at nodes of the concurrent elements. This displacement field enables to deform the current mesh, including within holes, so that the continuity of the mesh is preserved. Displacement, stress, strain, and von Mises stress fields, calculated at the Gaussian points of each element, are used to monitor the deformation process.

2.3. Convergence Criterion

SPECFEM2D uses the Courant-Friedrichs-Lewy (CFL) convergence condition for the resolution of the partial differential wave equations. This dimensionless number v is defined for an n dimension space as follows, with dt the temporal interval or sampling rate, Vxi the wave speed in direction xi, and the dimensional interval Δxi, which is the characteristic length of the spectral elements in a given direction:

$$v = dt \sum_{i=1}^{n} \frac{Vxi}{\Delta xi} \tag{1}$$

According to De Basabe and Sen (2010), the upper boundaries v_{max} of the CFL stability domains are tabulated for elastic or acoustic wave-propagation simulations, as a function of the temporal scheme chosen, and the number of Gauss-Legendre-Lobatto (GLL) points. Slight excess of that stability factor with respect to this upper bound v_{max} lead to spurious oscillations in the simulated signals. v_{max} depends on the explicit conditionally stable time schemes proposed in SPECFEM2D. Here we used the Newmark time stepping scheme so that the threshold retained is v_{max} = 0.5. Using a time step of $dt = 0.1 \cdot 10^{-9}$ s and 1,200,000 time steps leads to a maximum CFL stability condition of v = 0.06, which satisfies the requirements $v < v_{max}$ = 0.5. In the present work SPECFEM2D is configured to run in parallel mode on 20 processors (1.2 GHz each). Due to time-stepping parameters chosen to satisfy the convergence criterion, each wave propagation step is an 8-hr simulation. For the same model, the simulation is 8 times faster using this configuration, compared to a sequential simulation.

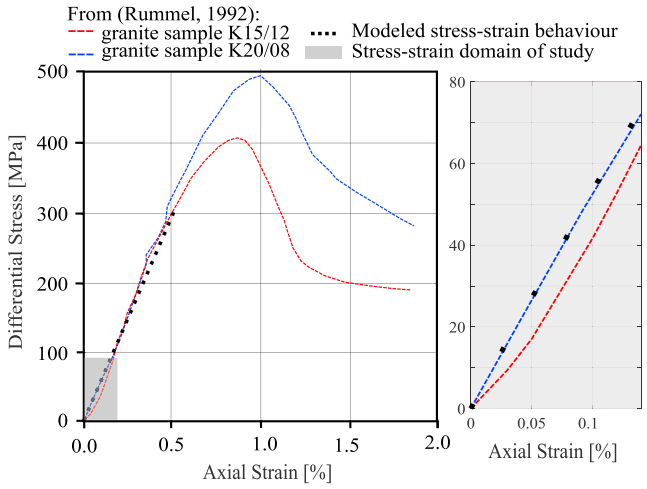

Figure 2. Stress strain behavior of granite sample subjected to constant confining pressure 40 MPa as a function of progressive axial strain, from Rummel (1992). The stress strain behavior obtained experimentally for two granite samples is superimposed to the stress strain behavior obtained from numerical simulation under the same condition with our effective sample. The effective medium intends to mechanically reproduce the behavior of a granite sample from Soultz-sous-Forêts in the rage of stresses considered in the experiments. The right insert shows a zoom in the zone of interest. The mechanical response of the effective sample represented in black dots depicts a perfectly elastic behavior with a Young modulus of 51 GPa which is close to the stress strain behavior obtained from the rock sample from Soultz-sous-Forêts. Mechanical response of the sample during the increasing imposed displacement. Stress is defined as the mean stress measured on the nodes of the upper loading line. Strain is calculated as the macroscopic uniaxial strain (relative variation of height). The dotted line is a perfectly elastic behavior with a Young modulus of 51 GPa smaller than the modulus of the rock matrix (54 GPa).

Code_Aster is also configured to calculate in parallel mode but on only four processors, using version 11.5.0, which is the current stable exploitation version. The CPU time of each job in *Code_Aster* is short, around 80 to 100 s, compared to the duration of the wave propagation simulation in SPECFEM2D (around 8 hr).

3. Mechanical Behavior and Scattering Properties

3.1. Macroscopic and Microscopic Mechanical Behavior

The mechanical behavior of the medium is characterized both at macroscopic and microscopic scales to ensure that the numerical simulation remains in the linear elastic domain. The macroscopic behavior is characterized by the stress-strain curve shown in Figure 2. At small imposed displacement the strain evolves linearly with stress which is the hallmark of linear elasticity. The slope provides an estimate of the apparent bulk modulus of the sample. Seven simulations were performed using *Code_Aster* for displacements δ in the range 0 to 150 μm. At the scale of the elements, the nodal forces and the vertical stress are computed along the upper boundary. When considering these displacements δ, the mean stress σ_{yy} ranges from 0 MPa to 70 MPa. The total force applied is computed as the sum of nodal forces calculated along the upper boundary. The stress at the macroscopic scale is then deduced from this measure of the total force. We assume that our sample is deformed under the small strain approximation. For a given displacement δ, we compute the macroscopic volumetric strain e_{vol} as the sum of the macroscopic component e_{YY} of the strain tensor and of its macroscopic component e_{XX}. The negative (compression) component e_{YY} is calculated as the relative elongation of each parallelepipedal sample along the vertical axis. With the initial high of the sample, noted h_0, $e_{YY} = \delta/h_0$. The macroscopic strain e_{YY} ranges from 0 to $1.4 \cdot 10^{-3}$ in our study. The positive component e_{XX} is estimated from the relative variation of width of the sample. According to this methodology, this component represents 38% in magnitude of the vertical component e_{YY}. To complement the deformation measurements, *Code_Aster* also allows the measurements of the relative variation of density $d\rho/\rho_0$ which is directly related to the volumetric deformation: $e_{vol} = dVol/Vol = -d\rho/\rho_0$ while deforming the medium, which will be used later in section 5.

Figure 2 compares the stress-strain behavior of two distinctive granite samples from Soultz-sous-Forêts, subjected to a constant confining pressure 40 MPa, as a function of axial strain (Rummel, 1992), to the stress-strain behavior of the effective medium simulated with *Code_Aster* under the same conditions (black dots). The right insert is a zoom in the stress-strain domain of the targeted stress-strain region of our study. It shows that stress evolves linearly with strain. An effective Young modulus of 51 GPa, smaller than the bulk modulus (54 GPa), is calculated from a linear regression of the computed data points presented in the figure (see Figure 2).

The two experimental curves illustrate the variability of the rock behavior. The clear superposition of our numerical results using the effective holed sample with the experimental behavior of the Soultz microfractured granite sample K20/08 fully supports the relevance of our numerical modeling in terms of mechanical behavior.

At the microscopic scale, that is, the scale of the elements, a Von Mises criterion is evaluated to check the relevance of a purely elastic modeling. Indeed, the Von Mises criterion is generally well suited to assess the elastic limit of the sample (Fanchon, 2001). The Von Mises equivalent stresses σ_{eq} are calculated at each quadrature point of each element and compared to the elasticity limit of the chosen material: R_e = 150 MPa (Harvey et al., 2005).

$$\sigma_{\text{eq}} = \sqrt{\frac{3}{2} s_{ij}.s_{ij}} \text{ with } s_{ij} = \sigma_{ij} - \frac{1}{3} Tr(\sigma)\delta_{ij} \quad (2)$$

The limit between the plastic and elastic domains is defined by $\sigma_{eq} = R_e$ so that $\sigma_{eq} < R_e$ corresponds to the elastic domain and $\sigma_{eq} > R_e$ to the plastic domain. For all the simulations done, we checked that max $(\sigma_{eq}) < R_e$ over all the Gaussian points of the element grid, showing that the explored stress field is far from the elastic limit with no significant concentration of stresses around the holes.

3.2. Seismic Source and Receiver

As presented in Figure 1a, a single seismic source is located at the middle of the left border of the block. Since SPECFEM2D computes only 2-D (*SH* and *P-SV*) wave propagation, the *P-SV* waves travel in the (*X*, *Y*) plane defined by the block and the *SH* wave travel in the *Z* direction, perpendicular to the (*X*, *Y*) (see Figure 1). As the code uses a plane strain approximation, the *P-SV* source is a line source along the direction perpendicular to the left border of the plate. Here we propagate a *SH* wavefield through the medium in order to consider a single polarization. The source time function is defined as a Ricker function of dominant frequency f_0 = 400 kHz, as shown in the left insert of Figure 1a.

In SPECFEM2D, receivers can be located at any nodes of the mesh grid. The particle motion at the receiver is recorded in three directions. We consider a single receiver facing the source and located at the middle of the block on the right boundary. This receiver can alternatively be shifted or duplicated to consider an *n*-receiver long line to monitor the spatial dependency along the boundary of the recorded seismogram. In order to assess the sensitivity of the measurement to the receiver position and to evaluate the spatial variability of the measurements, CWI calculations are performed using 32 receivers located along the sample boundary. In all treated cases, absolute locations of sources and receivers remain unchanged from the onset to the end of the deformation process.

3.3. Wave Diffusion and Mean Free Path

As previously mentioned in section 2.2, we introduced a set of holes in our effective medium to mimic the population of wave scatterers present in a natural granite rock. Our objective is to select a distribution of holes for the effective medium that best reproduces the scattering properties of a typical granite sample as the one presented in Figure 3. By varying the number, the size, and the locations of the holes, we are indeed able to control the scattering behavior of the effective medium. The coordinates of the holes are chosen randomly along the (*X*, *Y*) face of the block. To compare the scattering properties of the effective medium and the granite sample, we computed the mean free path of the medium (Olivier et al., 2015) which is defined as the mean distance between two diffusion events.

To assess the mean free path, we computed in the same manner as Wegler and Lühr (2001), the energy density $W(r, t)$ using the seismograms obtained either experimentally from an acoustic propagation in the granite sample or numerically for different distributions of holes in our effective medium, according to equation (3).

$$W(r,t) = \sum_{i=1}^{3} \left(f_i^2 + H(f_i)2\right) \quad (3)$$

Here f_i (in m/s^2), for *i* varying from 1 to 3, refers to the component of the acceleration and *H* the Hilbert transform. The observed energy density function $W(r, t)$ in J/m^3 is then compared to a wave diffusion model for body waves (i.e., the radiative transfer model), which allows to estimate the mean free path ℓ by least squares fitting as proposed in Olivier et al. (2015). As shown in Nakamura (1977) and Dainty and Toksöz (1977, 1981), the diffusion model expresses the seismic energy of multiscattered body waves $W(r, t)$ as a function of time and space as in equation (4).

$$W(r,t) = E_o \left(\frac{4\pi v_{ss}\, t}{3\eta_s}\right)^{-\frac{3}{2}} \cdot e^{\left(-\eta_i\, V_s t - \left(\frac{3r^2\eta_s}{4v_s\, t}\right)\right)} \quad (4)$$

where $W(r, t)$ is the energy density, E_0 the source energy, v_s the *S* wave velocity, *r* the distance to the source, η_i the intrinsic attenuation defined as the inverse of the intrinsic absorption characteristic length ℓ_a, and η_s the scatter attenuation which is the inverse of the mean free path ℓ.

By choosing an adequate reference in time t_1 and distance r_1 so that $W_1(r_1, t_1)$ = 1 J/m^3, and by taking the natural logarithm of a referenced function $U(t)$ defined below, equation (4) is linearized such that it relies

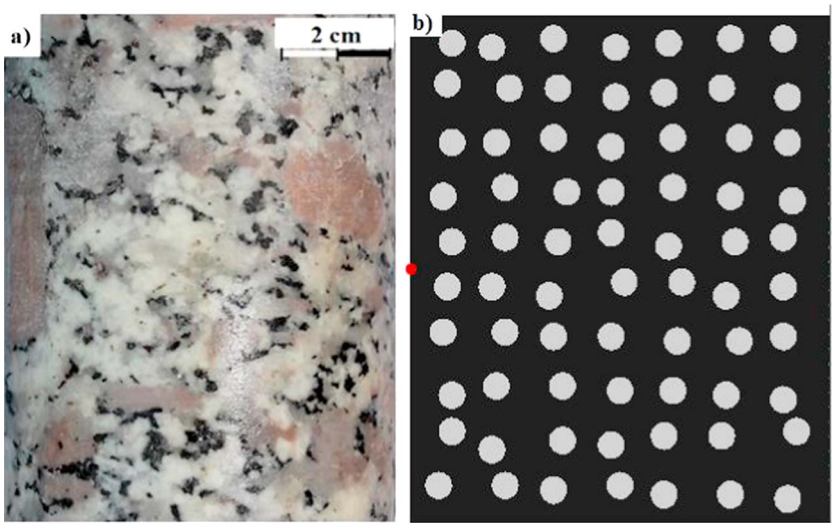

Figure 3. Modeling wave scattering in a granite sample. (a) Photography of a granitic sample obtained from a core through the Soultz-sous-Forêts deep geothermal reservoir at a depth of 3,790 m. The granite is a plutonic rock composed mainly of orthoclase feldspar, quartz, plagioclase feldspar, mica, and amphibole in which one can identify large crystallographic grains. Grains act as numerous scatters when the wavelength is at the order of the mineral size. We model the population of scatters as a set of cylindric holes (3 mm) randomly distributed in the sample (112 mm × 95 mm) as shown in (b).

on three dimensionless coefficients a_1, a_2, and a_3 expressed with parameters of the model (Wegler & Lühr, 2001). The linearized version of the energy density function is then

$$\text{Log } U(t) = a_1 + a_2 t + \frac{a_3}{t} \tag{5}$$

$$\text{with} \quad U(t) = \left(\frac{W(r,t)}{W_1}\right).\left(\frac{t}{t_1}\right)^{\frac{3}{2}}$$

$$\text{and } a_1 = \log\left(\frac{E_0}{W_1}\right).\frac{4\pi V_s\, t_1^{-\frac{3}{2}}}{(3\,\eta_s)}; a_2 = \eta_i V_s; a_3 = -\frac{3\eta_s\, r^2}{4V_s}$$

In particular, a_3 is expressed as a function of the intrinsic attenuation which is defined as the inverse of the mean free path.

$$\ell = \eta_s^{-1} \tag{6}$$

The energy density functions $W(r, t)$ computed from the seismograms using equation (3) are then linearized by multiplying them by the geometric factor $t^{3/2}$ and by taking the natural logarithm of both sides, which reconstruct the left side of equation (5). Finally, a least squares fitting is applied using equation (5) to estimate the dimensionless coefficients a_1, a_2, and a_3. The mean free path is inferred from the value of a_3, with Vs = 2,888 m/s and r = 0.95 mm, using equation (6). Figure 4 presents an example of this inversion procedure when considering an effective medium with 70 holes with 3 mm radius. The linearized energy density functions obtained for the effective medium and the granite sample are plotted together with the least squares regressions using equation (5).

The quality of the fit using equation (5) is a measure of the diffusion property of the wavefield propagation through the effective medium. To find the best parametrization of the implemented scatterers in the effective medium, we performed an inversion of the energy envelop measured from a real granite sample, using a grid search approach exploring multiple scatterer configurations defined by the number n of holes, their radii, and their locations. The modeled radiated energy for each configuration of scatterers and that obtained from the granite sample are compared as shown in Figure 4. The objective function used is the normalized mean square error or coefficient of multiple determination commonly named "r square" and noted r^2 presented in equation (7).

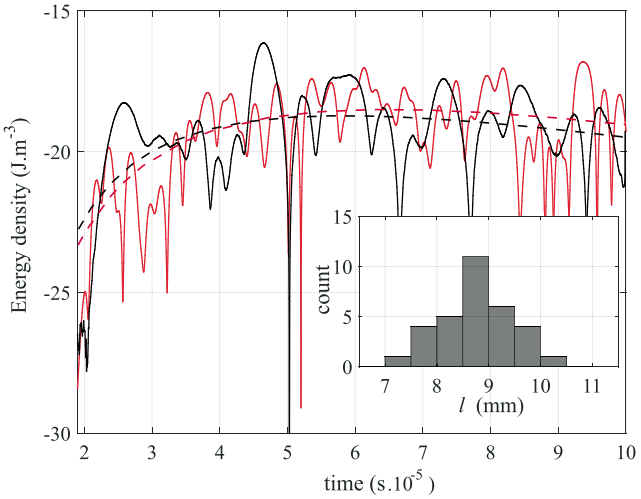

Figure 4. We characterize the scattering in the effective medium and in the granite medium with a simple diffusing model by calculating the linearized energy density functions $W(t)$ in both cases. The comparison shows the efficiency of the effective medium to describe the scattering happening in the granite sample. The least squares regression performed on the modeled function enables to check that the wave scattering properties are relevant by measuring the mean free path ℓ. The insert shows a histogram of the mean free paths values ℓ calculated at each of the 32 receptors equally distributed along the plate side.

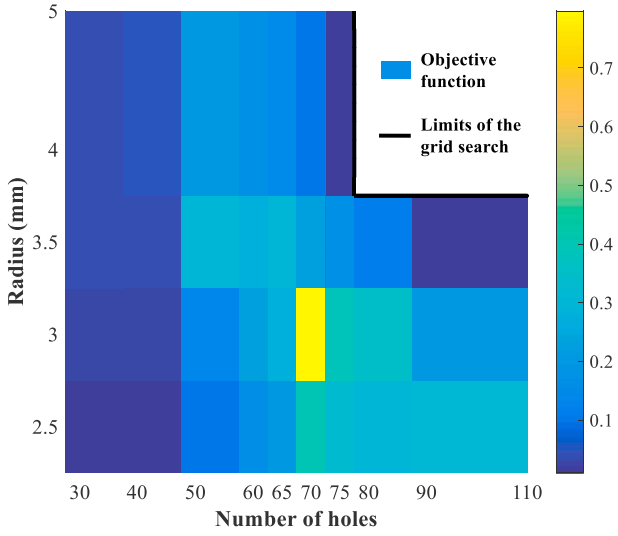

Figure 5. Grid search performed for nonoverlapping holes with radius ranging from 2.5 to 5 mm, which could be realistic sizes of grain inclusions in a rock mass. Number n of holes varies from 25 to 110. The color bar represents the objective function obtained for the comparison of each pair of radiated energy function (i.e., modeled for an effective medium and obtained in the granite sample). The objective function is maximized when considering 70 holes with radius of 3 mm.

$$r^2 = 1 - \frac{\|x_{ref} - x\|2}{\|x_{ref} - \overline{x}\|2} \tag{7}$$

In this equation, x_{ref} is a reference vector, x the outcomes, and $\|$ indicates the L2 norm of a vector and $\overline{x}$ its mean.

The grid search is performed for holes with radius ranging from 2.5 to 5 mm, which could be realistic sizes of grains inclusions in a rock mass. The lower limit of the considered range is chosen such that it ensures a sufficient discretization of the holes, when considering the characteristic length of the spectral elements l_c used in the study. Their number n varies from 25 to 110. The results of the grid search are presented in Figure 5. For each configuration, it shows the value of the objective function using equation (7). When increasing the percentage of holed surface, the holes are necessarily brought closer. The grid search is subsequently bounded in order to consider nonoverlapping holes. The objective function is maximum when considering 70 holes with radius of 3 mm for which the energy density function is presented in Figure 4. The scattering behavior of this effective medium is shown to be comparable to the one obtained for the laboratory sample and, as a result, will be used following this work.

The application of CWI requires the development of the diffuse wavefield at the receivers. The estimation of the mean free path also enables to assess the development of a multiscattering regime for the configuration retained. Multiscattering appears when the wave front emitted from the source sees the heterogeneities several times before reaching the receiver. It typically happens when the wavelength λ is of same length or shorter than the heterogeneity size d. Here the wavelength λ = 5.8 mm is estimated using the central frequency of the Ricker source and the S wave velocity. Strong scattering is assessed when the mean free path ℓ, the size of the defects d (varying here from 5 to 10 mm), the size of sample D (here 95 mm), and the wavelength λ satisfy the inequality: $\lambda \leq d \leq \ell < D$ (Planès & Larose, 2013). Here we neglect attenuation effects and we do not consider in the inequality the intrinsic absorption characteristic length ℓ_a, which appears in the inequality proposed by Planès and Larose (2013). The mean free path inverted for the best effective medium (70 holes with 3 mm radius) is ℓ = 8.8 mm, which satisfies the inequality. In addition, the goodness of fit in the least squares regression, between the modeled energy density function and the one computed with the recorded seismograms, is of r^2 = 0.89, when compared to the one obtained for other configurations. Our choice of effective medium thus satisfy all required parameters to apply CWI: (1) it is good analogue to actual granite sample, (2) it allows the propagation of multiscattered waves, and (3) the energy density function obtained from the seismograms is well fitted using a linearized form of a diffusion model.

In order to assess the sensitivity of the measurement to the receiver position, the variability of the inverted mean free path ℓ is evaluated when changing the receiver position along the sample boundary. We compared for the same distribution of scatters (i.e., holes), the inverted value of ℓ using the same least squares fitting process when considering 32 distinctive receiver positions equally distributed along the opposite side to the source. The insert in Figure 4 shows the histogram of the mean free path value ℓ calculated for each receiver position. The mean

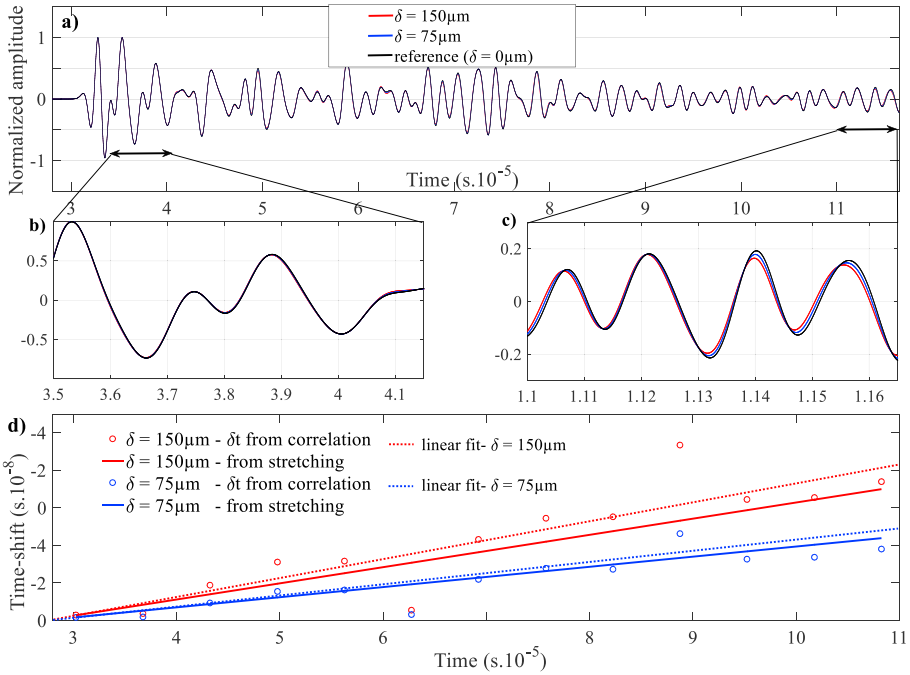

Figure 6. Coda wave interferometry. (a) Comparison of three synthetic waveforms recorded respectively for an imposed displacement $\delta = 0$ μm (black), $\delta = 75$ μm (blue), and $\delta = 150$ μm (red); (b) zoom in a 6.5 μs window of the waveform at the beginning of the coda where a negligible time shift is observed and (c) a zoom at the end of the waveform where the time shift is clearly sensitive to the imposed displacement. In Figure 6d, those time shifts within the coda are measured with either a time window correlation technique (circles) or a frequency stretching technique (solid line) when comparing waveforms at 75 and 0 μm displacement (blue) and at 150 and 0 μm displacement (red). The lines fitted on the time shifts measured by a time window correlation technique (circles) allows to measure a relative time shift $\varepsilon = \delta t/t$.

free path is 8.8 mm, and the standard deviation is 0.69 mm showing that the mean free path is weakly sensitive to the receiver position (8%).

4. Coda Wave Interferometry

We showed in the previous section that the scattering occurring in our so-called "effective medium" reproduces the scattering properties of a typical granite sample. In addition, we verified that the propagation medium creates a diffuse wavefield for late parts of the coda, which allows the use of CWI. In the following, we present two CWI methods that are applied to a given receptor to measure the relative time shifts within the coda of the signals along with an estimation of the related uncertainties. Both methods are then used to study the variation of relative time differences in the coda with strain, highlighting the elastic effect of an imposed deformation.

4.1. Two CWI Methods

We recall that the "reference" waveform is the one computed for a zero imposed displacement, and the "perturbed" waveform is calculated for a nonzero imposed displacement (Figure 6). For early times in the coda signal (Figure 6b), the reference and perturbed waveforms are similar because this part of the signal corresponds to weakly diffused phases that include few scattering events and accordingly correspond to quasi-direct wave path that have poorly sampled the medium. At later times, wave paths are longer owing to multiple scattering, which increases the sensitivity to the medium perturbations. This late part of the signal shows a clear time shift when increasing the imposed displacement, ranging typically from a few nanoseconds to a few tens of nanoseconds (Figure 6c).

We use two different methods to measure the observed time shifts along the coda by comparison of the reference and perturbed waveforms recorded at the receiver located at the middle of the right face of the plate (Figure 6d). First, we use a stretching approach of the whole signal (Sens-Schönfelder & Wegler, 2006). Second, we use a local method performed on consecutive fixed time windows based on cross-correlation of the signals to evaluate the time delays at different times t in the coda. The method

was introduced in Poupinet et al. (1984) and further developed in Snieder (2002). In both cases, one needs to take a special care on the frequency content of the compared signals.

For the stretching technique, Sens-Schönfelder and Wegler (2006) propose to estimate the relative time difference $\varepsilon = \delta t/t$ in the late part of the signal as the factor by which the time axis of one of the traces must be stretched or compressed to obtain the best correlation with the other trace. In this technique, one defines a "stretched" version of the reference signal: $S(t) = R((1 + \varepsilon)t)$, given the coefficient of stretching ε. Several stretched waveforms calculated for different stretching coefficients are compared by cross correlation with the reference signal. The quality of the fit is quantified by the correlation coefficient, noted r^2 and normalized so that the autocorrelation (i.e., the correlation of the signal with itself) leads to a coefficient equal to 1. This measures how successfully the stretched seismogram explains the variation of the reference seismogram. The stretching coefficient maximizing the correlation coefficient is retained. In our study, the maximal correlation coefficient r^2 is systematically higher than 0.997, which indicates that the stretched seismogram explains more than 99.7% of the total variation in the reference one.

For the correlation method, two signals are compared using cross correlations of successive time windows defined along the coda. Considering two signals *Ux* and *Uy*, cross-correlation factors measure the similarity between *Ux* and shifted copies of *Uy*, as a function of the time shift. The cross-correlation function obtained is normalized so that the autocorrelation equals 1 when no shift is applied. The lag or time shift leading to maximize the cross-correlation factor is an estimate of the time shift between the two signals. The correlation R_{UxUy} factors without normalization, for lags m in [-N, N] with N the maximal lag, are given by

$$R_{UxUy}(m) = \begin{cases} \sum_{n=0}^{N-m-1} Ux_{n+m} Uy_n^*, & m > 0 \\ R_{UyUx}(-m), & m < 0 \end{cases}, \tag{8}$$

and the correlation function has elements c given by

$$c(m) = R_{UxUy}(m - N), m = 1, 2, \ldots, \quad 2N - 1 \tag{9}$$

The reference ($\delta = 0$ μm) and perturbed waveforms (given displacement δ) are compared using cross correlation in successive nonoverlapping windows defined after the first arrivals. In principle, a single lag measure δt_i, at a time t_i, is sufficient to estimate the relative time shift $\delta t_i/t_i$ if δt/t is supposed to be constant. However, the error on the relative time shift estimation evolves with the square inverse of the number of time shift estimations and thus the number of successive windows (Clarke et al., 2011). To improve the estimation of the relative time shift $\varepsilon = \delta t_i/t_i$, we consider successive distinctive estimations of the time shift δt. Figure 6d shows with solid dots the absolute time shift δt_i measured for two different displacements (δ = 75 μm and δ = 150 μm) with respect to the reference waveform at zero displacement ($\delta = 0$ μm). The increase of the time shift along the coda is estimated by a linear regression which provides an average slope or an average relative time shift $<\delta t_i/t_i>$. In order to improve the picking of the time delays, we used a two-step correlation strategy in which the reference signal *f*1 and perturbed signal *f*2 are first correlated to obtain a correlation function *g*1. *g*1 is then correlated with the autocorrelation function *g*2 of the perturbed signal. This approach allows to use a priori estimates of the time shifts when correlating *g*1 and *g*2. It also improves signal-to-noise ratios and add redundant information that increases the accuracy of the time shift measurements. More details and synthetic tests can be found in the supporting information.

Parameters of the windows used in the CWI method, such as the number of discretization points, its duration, and its frequency content, deeply affect the ability to assess the time shift measured in each window. Several tests—detailed as supporting information—show the problems that may emerge during the correlation process when considering insufficiently discretized windows to estimate time shifts. As explained in the supporting information, we choose to fix the length of the signals (120 μs) and the sampling rate (10^{-10}) due to their influence on the computational time of our numerical simulations. The correlation method is applied on 6.5-μs-long windows containing 65,000 points each and filtered in a high-frequency range [1,000, 1,100] kHz to improve the accuracy of the CWI method.

4.2. CWI Accuracy

It is necessary to assess the accuracy of the time shift measured with the two CWI methods as well as their spatial variability in order to study statistically significant effects produced when varying parameters of the

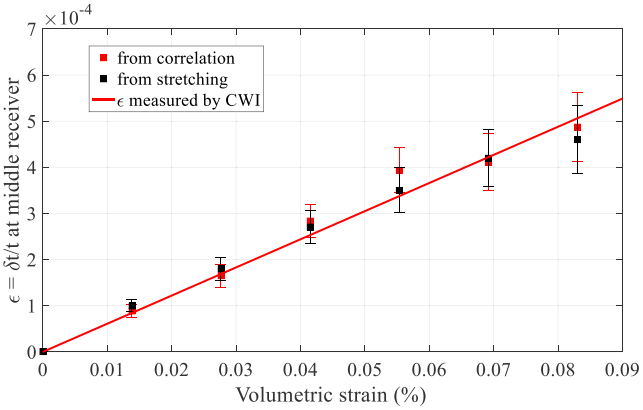

Figure 7. Evolution of the relative time shift ($\varepsilon = \delta t/t$) measured from waveforms of deformed samples using either the stretching technique (black) or the time window correlation technique (red) as a function of the macroscopic volumetric strain, in percent ($e_{vol} = e_{XX} + e_{YY}$). The relative time shifts are measured from signals acquired at the middle of the right border of the plate with one receiver. The bars account for the error on the measure of the relative time shift, estimated for each coda wave interferometry (CWI) method, according to section 4.2. For both CWI methods, we see a clear linear behavior (red line): $\delta t/t = -0.69\ e_{vol}$.

simulation (see section 5). We focus first on the CWI method using cross correlation of windowed signals to estimate distinctive time shifts in the coda depth. The relative time shift is obtained from a linear regression on the time shifts. The error is evaluated as the uncertainty around the slope parameter. Let E be the random variable corresponding to the estimated slope value, and its observed value is ε. Its variance is calculated as a function of the variance of the residuals s_r^2 and the standard deviation of the n data points X as $s_E^2 = s_r^2/(n \cdot \sigma_x^2)$. The random variable $T = (\varepsilon - E)/s_\varepsilon$ follows a Student law of order $n - 2$. As a result, it is possible to calculate a confidence interval for the slope, IC, such that $IC = [a - t_{1-\alpha/2} s_\varepsilon,\ a + t_{1-\alpha/2} s_\varepsilon]$. The standard deviation on the slope parameter (i.e., the relative time shift) is measured for each linear regression, at a given displacement δ. It is typically $0.4 \cdot 10^{-5}$, and it increases with δ. It represents 10% to 15% of the relative time shift measured, and it is represented by the error bars on the red squares in Figure 7. This is a measure of the sensitivity of this estimating method enabling to distinguish which parameter in the simulation has a statistically significant effect on the relative time shift measured.

For the stretching technique, the relative time shift is measured by comparison of a stretched perturbed signal with the reference signal. The method is applied on the whole coda length. In order to assess the error on the value of ε, we build a population of relative time shifts by applying the method on pair of reference-perturbed signals whose length is reduced from their end, from their beginning, or from both ends. Application of stretching technique on these signals allows to create a Gaussian distribution whose standard deviation is then calculated. This result is obtained for the comparison of a reference and perturbed seismograms for every considered displacement δ. The standard deviation on the relative time shift evolves in the same fashion as for the error on the correlation technique described in the previous paragraph. It is typically $0.33 \cdot 10^{-5}$ for $\delta = 75$ μm, and the mean value for all the displacements is $0.4 \cdot 10^{-5}$. It also represents from 10% to 14% of the relative time shift ε measured from this technique, and it is represented by the error bars on the black squares in Figure 7.

To complete the study of the error on the measurement of the relative time shift, we analyze the spatial variability of the measurements. CWI methods are applied on signals recorded on 32 distinctive receivers equally distributed along the plate border. The dispersion of the population of distinctive estimations varies with the displacement δ imposed. The standard deviation, typically of $0.5 \cdot 10^{-5}$, increases with the displacement and represents from 14% to 16% of the relative time shift difference when δ increases from 25 to 150 μm. The spatial variability measured for each relative time shift estimation is represented with bars in Figure 8. The time shifts spatial variability within our effective medium is thus in the order of the uncertainties associated with a single deterministic path.

4.3. CWI and Mechanical Strain

We perform the CWI for successive displacement δ to monitor how strain impacts the time shifts measured in a coda depth and the value of the relative time shift. Figure 6d shows the variation of time shifts estimated in successive window in a coda depth, for two loading conditions, that is, $\delta = 75$ μm and $\delta = 150$ μm. Time shifts are measured either with the time window correlation technique (circles) using 6.5 μs long windows or using the stretching technique (solid line). While doubling the imposed displacement, the maximum time shift recorded in the coda nearly doubles (from $-1.95 \cdot 10^{-8}$ to $-3.87 \cdot 10^{-8}$ s). The slope of the linear regression and the estimation of the relative time shift ε increases with displacement which is depicted in Figure 6d. This figure shows that $\varepsilon = -2.8 \cdot 10^{-4}$ for the correlation technique and $\varepsilon = -3.2 \cdot 10^{-4}$ for the stretching method, for $\delta = 75$ μm. When doubling the displacement (i.e., for $\delta = 150$ μm), $\varepsilon = -4.3 \cdot 10^{-4}$ for the correlation technique and $\varepsilon = -5.3 \cdot 10^{-4}$ for the stretching method.

Figures 7 and 8 show precisely how the relative time shift, measured with both techniques, evolves as a function of the displacement and strain. In Figure 7, the relative time shifts are measured by applying the

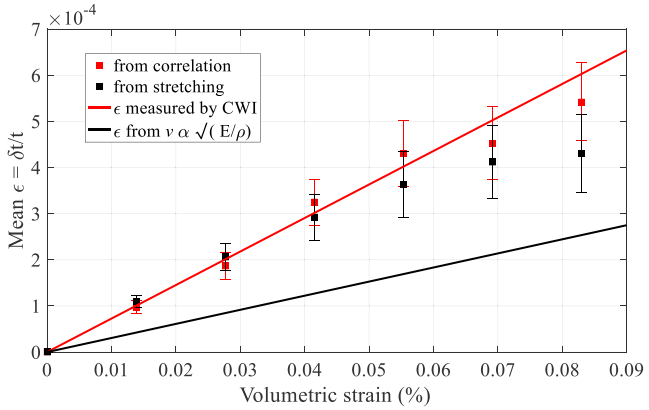

Figure 8. Evolution of the relative time shift ($\varepsilon = \delta t/t$) measured from waveforms of deformed samples using either the stretching technique (black) or the time window correlation technique (red) as a function of the macroscopic volumetric strain, in percent ($e_{vol} = e_{XX} + e_{YY}$). The relative time shifts are obtained from a spatial homogenization by averaging the 32 distinctive ε measured from receivers located along the right plate border. The bars account for the standard deviation of the spatial variation on the measurements. For both coda wave interferometry (CWI) methods, we see a clear linear behavior (red line): $\delta t/t = -0.71\ e_{vol}$. The relative wave speed variations expected due to the squirt law linking wave speed and density are plotted along in black to discuss the relative weight of each contribution in the observed delays.

CWI method on a single receiver located at the middle of the plate border. Figure 8 presents the mean relative time shifts obtained by averaging distinctive ε obtained with signals acquired by 32 receivers equally distributed along the right border of the plate. In each figure, the measurements are carried out for seven distinctive displacements ranging from 0 to 150 μm. When measuring relative time shifts at the receiver (Figure 7) or when measurements results from a spatial average (Figure 8), the results of both CWI methods match, which shows the consistency of those techniques. With $\Delta\varepsilon$ the difference between the values estimated with both methods, the mean difference for the calculated values of ε is $\underline{\Delta\varepsilon} = 0.15 \cdot 10^{-4}$, which is low compared to the magnitude of this relative time shift and to the error on the measurements, estimated in the previous paragraph. Note that the difference between the relative time shifts estimated from both methods increases with displacement, which could be explained by the increase with imposed displacement of the error estimated on ε for each method (see section 4.2).

The main result of Figures 7 and 8 is the linear evolution of the relative time shift with strain, which demonstrates that CWI is sensitive to mechanical strain. The linear regression performed with the data obtained from the middle receptor leads to the following relation: $\delta t/t = -0.69\ e_{vol}$ (Figure 7). The relative time shifts obtained from the spatial homogenization over the side boundary is also well fitted by a linear law: $\delta t/t = -0.71\ e_{vol}$ (Figure 8). Both linear behaviors show that the amplitude of the relative time shift is a proxy of the macroscopic strain. Note that the wave speed is a fixed parameter in our simulations while the displacement δ, the strain ε, and the stress state vary. Our study highlights that the time shifts measured in the coda carry a real deformation signal. Meanwhile, a volumetric change of the medium during the compression will result in an increase in density and subsequently in a velocity change. Inclusion of relative time shifts expected from the squirt law linking wave speed v and density ρ (black line in Figure 8) allows us to discuss the influence of the medium density changes on the CWI measurements later, in section 5.2.

5. Discussion

To ensure that the observed evolution of the coda of the seismograms during mechanical loading carries a deformation signal, several tests need to be performed to check that the CWI assessments (relative time shift measurements) are not actually influenced by the simulation parameters such as the source characteristics, the sampling rate, or related numerical biases.

5.1. Influence of Source Parameters and Time Resolution

We first tested if the relative time shift estimated from CWI methods could depend on the central frequency of the source. For this, we compare the relative time shifts measured for two different values of the source central frequency f_0 = 400 kHz and f_0 = 100 kHz. The relative time shift is measured in these two cases for distinctive displacements δ varying from 0 to 150 μm. Because the cross-correlation method is sensible to the frequency content of the signals compared, we look in each case for a similar number of wavelengths in each window. As a consequence, the windowed-signals are filtered in the range [250 kHz; 350 kHz] when considering the 100 kHz central frequency source and in the range [1,000 kHz; 1,100 kHz] when considering f_0 = 400 kHz. The average relative time shifts measured with both methods for a 75 μm displacement are ε (f_0 = 400 kHz, δ = 75 μm) = $-3.1 \cdot 10^{-4}$ and ε (f_0 = 100 kHz, δ = 75 μm) = $-2.8 \cdot 10^{-4}$. The difference $\Delta\varepsilon_{f0}(\delta = 75\ \mu m) = \varepsilon\ (f_0 = 400\ kHz, \delta = 75\ \mu m) - \varepsilon\ (f_0 = 100\ kHz, \delta = 75\ \mu m) = 0.3 \cdot 10^{-4}$ is of more than 1 order of difference compared to the mean relative time shift obtained from ε (f_0 = 400 kHz, δ = 75 μm) and ε (f_0 = 100 kHz, δ = 75 μm). Such a result is obtained for each displacement δ in [0, 25, 50, 75, 100, 125, 150] μm and

$$\sum_{\delta} \| \frac{2.\Delta\varepsilon_{f_0}(\delta)}{\varepsilon(f_0 = 400\ \text{kHz}, \delta\ ) + \varepsilon(f_0 = 100\ \text{kHz}, \delta)} \| \approx 0.07$$

Moreover, the difference is of the same magnitude as the error on the measurements previously estimated. When compared to the uncertainty on the estimation evaluated for both CWI methods in section 4.2, or to the spatial variability on the measurement, we conclude that this change in the source parameters has a statically insignificant effect on the measurements.

We also checked the influence of a change in the sampling rate. The error on the time shift $e_{\delta t}$ estimated in each successive window evolves with the square inverse of the number of discretizing points considered in each window (Clarke et al., 2011; Weaver et al., 2011). The decrease of the sampling rate, with a fixed length of signal, increases the error on the time shift because it diminishes the number of discretizing points in a window. The relative time shift is estimated in the same way as for the analysis of the source influence, with two sampling rates: the current sampling rate (dt = 0.1 ns) and a lower sampling rate (dt = 0.8 ns). The mean relative time shifts measured for a 75 μm from correlation technique and stretching method, for the high sampling rate, is ε (dt = 0.1 ns) = $-3.1 \cdot 10^{-4}$. It is ε (dt = 0.8 ns) = $-3.0 \cdot 10^{-4}$ when a coarser sampling rate is used. The difference in the measured value obtained by changing this source parameter is also insignificant compared to the dispersion due to the spatial localization of the receiver or compared to the error on the estimation method. As for the central frequency, we compare the differences between the measured relative time shifts, at two different sampling rates, to their mean value, for every considered displacement:

$$\sum_{\delta} \| \frac{2.\Delta\varepsilon_{dt}(\delta)}{\varepsilon(dt = 0.1\text{ns},\ \ \delta\ ) + \varepsilon(dt = 0.8\text{ns}, \delta)} \| \approx 0.01$$

This source parameter has an insignificant influence on the measures. It shows that even if the error on the estimation of the time shifts is higher, the estimate from linear regression of $\varepsilon = \delta t/t$ still remains consistent. As a result, the relative time shifts measured from CWI are not influenced by a change of the source parameters or of the model. They carry a real deformation signal.

5.2. Physical Interpretations of CWI Time Shifts

Time delays in seismograms are induced by changes of physical properties such as wave velocities, anisotropy, temperature gradient, stresses changes, or evolving scattering properties (Stehly et al., 2007). However, the causal link between observed time delays in seismograms and physical processes at play in situ is often complex and not unique involving generally ad hoc multiscale integration because of the numerous Earth structure heterogeneities. Time shifts measured by CWI follow the same difficulties. They encompass all the physical sensitivities of diffuse wavefield including reversible or irreversible phenomena. Typically, their interpretation is carried out in the frame of a given model, but the uniqueness of the model is rarely demonstrated. To illustrate this difficulty, this section intends to discuss the interpretation of the relative time shifts measured in our study in a sort of blind test of two classical models: the first one is the most used and interprets time delays as the results of irreversible wave velocity variations typically related to damage development in the sample (e.g., microcracks); the second model is more specific to reversible time delays and relies on acoustoelastic effects responsible for seismic velocity changes due to reversible stress perturbations because of nonlinear rheology (Aoki, 2015).

The first framework is the interpretation of CWI measurements as small variations of seismic velocities owing to several factors such as water saturation related to rainfalls, air pressure, stress or temperature changes, and microcrack developments (Lockner et al., 1977; Planès & Larose, 2013; Snieder, 2002). This classical approach follows the work of Snieder et al. (2002) which is often introduced when using coda waves to monitor weak changes in solids. Given a wave diffusion record which is conceptualized as the superposition of wave packets arriving with random time and amplitudes, time delays are supposed to be induced by a global velocity change $\delta v/v$. This model is built on several assumptions. The relative velocity change is assumed to be homogeneous in the medium. The amplitude of the wave packets is constant such that the positions of the source and scatterers are unchanged. As a consequence, the effects of deformation on the wave diffusion are neglected, and relative time shift $\delta t/t$ is proportional to the relative velocity change $\delta v/v$: $\varepsilon = \delta t/t = -\delta v/v$ (Planès & Larose, 2013). Indeed, deformation effects are generally considered as a few orders of magnitude lower than the velocity effect that are typically related to damage development in the sample (e.g.,

microcracks). As an illustration, Yamamura et al. (2003) shows a 3 orders of magnitude difference between strain and relative time changes $\delta t/t$, which is of the order of 10^{-3}. Yamamura's work is built on the analysis of a 1-year compressional wave velocity and attenuation data set, acquired continuously across 12 m in a vault at the coast of Miura Bay, Japan (Yamamura et al., 2003).

By applying such a formalism to our numerical results, the relative time shifts measured in our study would be the result of pure velocity changes. The maximum relative time shift ε measured when applying a displacement $\delta = 150$ μm ($v_s = 2{,}888$ m/s) would result in a relative velocity change of $\delta v/v = 4.7 \cdot 10^{-4}$ and an amplitude of the velocity variation of about $\delta v = 1$ m/s. It is of interest to note that this value is in the order of magnitude of velocity changes classically found in various tectonic environments (Brenguier et al., 2008) or experimental results (Planès & Larose, 2013). Clearly, this model is not appropriated for our study since wave velocities are kept constant all along our simulations and reversible time shifts are observed.

Moreover, relative time shifts are shown to be directly related to the linear elastic deformation of the sample which proves that the amplitude of the relative time shift is a proxy of the macroscopic strain, as presented in section 4.3 (see Figures 7 and 8). A theoretical model based on the elastic coupling between scatterers has still to be developed to justify this interpretation.

We assume here the wave speed to be constant, while the volumetric change of the medium during the compression will result in an increase in density and subsequently in a velocity change. Actually, it is necessary to take into account the influence of the medium density changes on the CWI measurements. With a bulk modulus E and a constant K proportional to Poisson's ratio, elastic wave velocities v and density ρ are related according to the following relation:

$$v = K.\sqrt{E/\rho} \tag{10}$$

Differentiating equation (10) leads to $\delta v/v_0 = 1/2 \cdot \delta\rho/\rho_0 + 1/2 \cdot \delta E/E$. Assuming a constant bulk modulus and a constant mass and introducing the volume of the sample Vol, one obtains $\delta v/v_0 = 1/2 \cdot \delta Vol/Vol_0$. Finally, if we assume a little deformation of the sample, such that the relative variation of volume equals the volumetric strain e_{vol}, we finally get the relation (11):

$$\delta t/t = ½ \cdot e_{vol} \tag{11}$$

This is the so-called time dilation/contraction model. In order to discuss the influence of the medium density changes on our CWI measurements, Figure 8 includes the linear trend of equation (11) derived above. We see from Figure 8 that our numerical results fitted by the red line with a slope of 0.7 are not consistent with the time contraction/dilatation model (black line) for which the slope is 0.5. It shows that relative traveltime shifts induced by density effects explain only about half the CWI signal measured in our simulation but not all of it. To explain this discrepancy, we suggest that two important effects are neglected in the time contraction/dilatation model: first, the spatial heterogeneity of the strain tensor in particular around the scatterers, and second, deformation is not purely volumetric during our uniaxial compression.

Another formalism to interpret changes of seismic velocities induced by stress perturbations is acoustoelasticity. In this framework where nonlinear elastic laws are considered, motion equations predict that wave velocities and strain—or stress—depend on one another. This coupling is invoked to explain the effect of static stress on the propagation velocities. For example, Aoki (2015) suggests that the temporal changes of physical properties can result from variability of third-order elastic moduli that arise during stress-induced deformation of the medium. Indeed, if one considers a nonlinear elastic material, the velocity of longitudinal and transversal waves, v_p and v_s, will deviate from their initial values according to the theory of acoustoelasticity involving second- and third-order elasticity constants (Hughes & Kelly, 1953; Sneddon & Murnaghan, 1954). In the particular case of a medium submitted to a uniaxial normal stress σ_{yy}, and in the range of the stress changes considered in our approach, one can simplify the acoustoelastic equations so that these equations follow a linear relationship between the relative time shifts and the applied uniaxial stress (Shokouhi et al., 2012). In this particular framework, reversible time shifts are due to reversible strain changes and the measured relative time shift ε is shown to be proportional to the strain. Noticeably, this linear relation between time shift and strain is similar to our observations even if this relation in our simulation is not produced by an acoustoelastic effect given that this specific rheology is not included in our simulation. Indeed, elastic parameters of our model are invariant with stress or strain.

5.3. Implications for Ambient Seismic Noise Monitoring

Interferometry techniques have found a large range of applications over the past years. When applied to coda waves reconstructed with ambient seismic noise, this technique has found a significant application for monitoring structures at various scales. Examples include monitoring of volcanoes, mud landslides (Brenguier et al., 2008, 2011; Duputel et al., 2009; Mainsant et al., 2012), and also a geothermal reservoir in the area of Rittershoffen (northeast of France) where a deep geothermal plant (2,500 m) is installed (Lehujeur et al., 2014, 2017). As discussed above, the physical causes at the origin of the relative time shifts are multiple and complex and require different models to interpret the CWI measurements. The specificity of our study is the constant wave velocity and the interpretation of the relative time shifts as a deformation signal. The identification of a deformation signal in the CWI measurements provides new outcomes for the use of this interferometry technique in monitoring stress changes. The measured relative time shifts of magnitude close to the strain could be interpreted in the field by slight changes in the stress state in a reservoir rock mass. Such enhanced interferometry technique could interestingly be applied to seismic activity monitoring or to track the propagation of a hydraulic fracture. It could detect stress changes linked to a reservoir stimulation as a fracture advance through a formation. The high resolution and strong sensitivity of CWI could thus lead to a highly sensitive monitoring technique enabling to control the changes occurring in the stress state of the surrounding medium at depths.

However, even if the identification of a deformation signal in the CWI signal represents an interesting step for the application of those techniques to monitor structures, several questions related to the interpretation of the measurements remain open. The discrimination between the different origins—changes of properties, such as velocity, attenuation, anisotropy, and scattering properties—of the delays measured with CWI type of signals is challenging. The deformation signal is in fact coupled with and associated to wave speed variations or amplitude variations (Obermann et al., 2013, 2014).

Such complex interaction between several physical quantities is illustrated in our simulations with the presence of small decorrelation and amplitude variations in the coda of the signals (see Figure 6c). In our case, the difference in the shape of the seismograms is slight, which is shown by the good correlation coefficient resulting from the stretching technique (see section 4.1). Both theoretical and experimental results have shown that amplitude variations or decorrelation measurements in the coda are related to changes in the diffusion properties of the medium and thus to structural changes in the medium (e.g., Larose et al., 2010; Michaels & Michaels, 2005; Rossetto et al., 2011). They thus differ from time shift presented here and also measured on the coda of signals. A more complete exploration of this decorrelation signal and the related role of the position of the scatterers through the simulation will be the focus of a later work.

Finally, the numerical approach presented in this work, which combines both elastic deformation and seismic wave propagation modeling, also opens new perspectives for direct comparisons of CWI measurements obtained in simulated cases with those computed for real laboratory experiments. Such comparisons could help to distinguish the different physical origin of the measured time shifts in various experimental configurations. Several studies are currently underway with an analogue experiment designed to measure the relative time shift in the same manner as in the numerical work presented in this study, following the setup displayed in Figure 1. The use of an experimental approach together with our numerical study would provide new outcomes to properly assess the relative contributions of deformation and velocity changes in CWI measurements.

6. Conclusion

CWI is a technique that estimates slight traveltime perturbations from a comparison of the coda waves before and after a perturbation. In particular, its application to seismic noise has been shown to be a useful technique over the last decade to monitor structures such as volcanoes, fault zones, or a geothermal reservoir in the area of Rittershoffen (northeast of France) where a deep geothermal plant (2,500 m) is installed (Lehujeur et al., 2014). Even if the seismic velocity changes appearing in the acquired signals are known to be a result of the change of several factors such as water saturation related to rainfalls, air pressure, and stress or temperature changes, it is generally challenging to interpret these temporal changes observed in records as disruptive events. Our work shows from a direct numerical modeling that deformation signal exists in CWI measurements.

This direct numerical modeling is obtained by combining a seismic wave propagation, modeled within a diffusive medium using a spectral element approach (SPECFEM2D), during an elastic deformation of the medium obtained from a finite element approach (*Code_Aster*). As an illustration, the effective propagation medium is a 112 × 95 mm plate simulating a granite sample in which 70 holes with radius of 3 mm randomly distributed in the homogeneous elastic block behave as scatterers. This distribution of scatters intends to simulate the behavior of a granite block with its inclusions of grains, typically encountered in the deep geothermal site of Soultz-sous-Forêts, France. The choice of the scatterer distribution is not trivial. We provide evidences showing that the linear elastic behavior of the propagation medium and the acoustic behavior of the medium satisfy the requirements for CWI to be applied. The mean free path inverted by comparison of the energy density function with a simple multiple diffusion model by least squares fitting (ℓ = 8.8 mm) satisfies the criterion necessary for strong scattering, and the computed function fits well the diffusion model. The wavefield propagated is sufficiently diffracted to show the appearance of time shifts in its late part between signals acquired for.

Time shifts in the coda depth of the signals are then quantified using two CWI methods: the results of the stretching technique computed on the whole signal are consistent with the results of a windowed cross correlation. The relative time shift measured along the coda signal shows to vary with the displacement imposed in a linear fashion. The increase of the relative time shift with strain shows that elastic deformation is fully correlated to time shifts. The use of two distinctive estimation methods which overlap show the consistency of the calculation of the time shifts. The parametrization of the cross-correlation method is tackled to increase its accuracy, and the spatial dispersion of the measurement is estimated along the right face of the plate to discuss the sensibility of the relative time shift. It is thus possible to discuss the independence of the estimation toward different parameters of the simulation by showing the statistical insignificance of the effects on the relative time shifts due to a variation of the source central frequency or of the sampling rate, for example. Our tests show that the time shifts measured in the seismograms carry a real deformation signal and are not numerical artifacts. A careful comparison with the contraction/dilatation model which takes into account the velocity variation produced by the increase of density during the compression revealed that this model explains only half of the measured relative traveltime shifts. To explain this discrepancy, we suggest that CWI is sensitive to the heterogeneity of the elastic deformation field in addition to the isotropic volumetric deformation and independently of nonlinear acoustoelastic effects. The reproducibility of the measurements also shows that this nondestructive monitoring method could be interestingly applied in the field, given that there is a CWI signal without damage. We introduced CWI, and in particular ambient noise interferometry, as a highly sensitive monitoring technique needing only few requirements but suffering from problems with the interpretation of measured signals. Our results might provide new outcomes for their interpretation and for the application of the technique.

Acknowledgments

This work has been published under the framework of the LABEX ANR-11-LABX-0050-G-EAU- THERMIE-PROFONDE and benefits from a funding from the state managed by the French National Research Agency (ANR) as part of the "Investments for the Future" program. It has also been funded by the EU project EU H2020 research and innovation program (grant agreement 691728 - DESTRESS). The authors would like to thank Olivier Lengline for his fruitful discussions, as well as Alain Steyer for technical support at the laboratory. We also thank Florent Brenguier, an anonymous referee, and Editor Andre Revil for constructive comments. For the use of SPECFEM2D, a free software downloadable at https://github.com/geodynamics/specfem2d.git, we thank the Computational Infrastructure for Geodynamics (http://geodynamics.org) which is funded by the National Science Foundation under awards EAR-0949446 and EAR-1550901. For the use of *Code_Aster*, which is also a free software downloadable at https://www.code-aster.org/V2/spip.php?rubrique7, we thank Electricité de France (EDF). Data displayed or used to generate figures and plots are accessible at http://dx.doi.org/10.25577/2018-AZZOLA-JGR.

References

Aki, K. (1969). Analysis of the seismic coda of local earthquakes as scattered waves. *Journal of Geophysical Research*, *74*(2), 615–631. https://doi.org/10.1029/JB074i002p00615

Aki, K. (1980). Attenuation of shear-waves in the lithosphere for frequencies from 0.05 to 25 Hz. *Physics of the Earth and Planetary Interiors*, *21*(1), 50–60. https://doi.org/10.1016/0031-9201(80)90019-9

Aki, K., & Chouet, B. (1975). Origin of coda waves: Source, attenuation, and scattering effects. *Journal of Geophysical Research*, *80*(23), 3322–3342. https://doi.org/10.1029/JB080i023p03322

Aoki, Y. (2015). Monitoring temporal changes of seismic properties. *Frontiers in Earth Science*, *3*, 42. https://doi.org/10.3389/feart.2015.00042

Boué, P., Roux, P., Campillo, M., & Briand, X. (2014). Phase velocity tomography of surface waves using ambient noise cross correlation and array processing. *Journal of Geophysical Research: Solid Earth*, *119*, 519–529. https://doi.org/10.1002/2013JB010446

Brenguier, F., Clarke, D., Aoki, Y., Shapiro, N. M., Campillo, M., & Ferrazzini, V. (2011). Monitoring volcanoes using seismic noise correlations. *Comptes Rendus Geoscience*, *343*(8–9), 633–638. https://doi.org/10.1016/j.crte.2010.12.010

Brenguier, F., Shapiro, N. M., Campillo, M., Ferrazzini, V., Duputel, Z., Coutant, O., & Nercessian, A. (2008). Toward forecasting volcanic eruptions using seismic noise. *Nature Geoscience*, *1*(2), 126–130. https://doi.org/10.1038/ngeo104

Campillo, M., & Paul, A. (2003). Long-range correlations in the diffuse seismic coda. *Science*, *299*(5606), 547–549. https://doi.org/10.1126/science.1078551

Campillo, M., & Roux, P. (2015). Crust and lithospheric structure—Seismic imaging and monitoring with ambient noise correlations. In G. Schubert (Ed.), *Treatise on geophysics* (2nd ed., pp. 391–417). Oxford: Elsevier. https://doi.org/10.1016/B978-0-444-53802-4.00024-5

Clarke, D., Zaccarelli, L., Shapiro, N. M., & Brenguier, F. (2011). Assessment of resolution and accuracy of the moving window cross spectral technique for monitoring crustal temporal variations using ambient seismic noise: MWCS: Assessment of resolution and accuracy. *Geophysical Journal International*, *186*(2), 867–882. https://doi.org/10.1111/j.1365-246X.2011.05074.x

Dainty, A. M., & Toksöz, M. N. (1977). Elastic wave propagation in a highly scattering medium—A diffusion approach. *Journal of Geophysics*, *43*, 375–388.

Dainty, A. M., & Toksöz, M. N. (1981). Seismic codas on the Earth and the Moon: A comparison. *Physics of the Earth and Planetary Interiors*, *26*(4), 250–260. https://doi.org/10.1016/0031-9201(81)90029-7

De Basabe, J. D., & Sen, M. K. (2010). Stability of the high-order finite elements for acoustic or elastic wave propagation with high-order time stepping. *Geophysical Journal International*, *181*(1), 577–590. https://doi.org/10.1111/j.1365-246X.2010.04536.x

Duputel, Z., Ferrazzini, V., Brenguier, F., Shapiro, N., Campillo, M., & Nercessian, A. (2009). Real time monitoring of relative velocity changes using ambient seismic noise at the Piton de la Fournaise volcano (La Réunion) from January 2006 to June 2007. *Journal of Volcanology and Geothermal Research*, *184*(1-2), 164–173. https://doi.org/10.1016/j.jvolgeores.2008.11.024

Fanchon, J. L. (2001). Guide de mécanique, Nathan.

Harvey, P. K., Brewer, T. S., Pezard, P. A., & Petrov, V. A. (2005). *Petrophysical Properties of Crystalline Rocks*. Geological Society, London, Special Publications, 240.

Hennino, R., Trégourès, N., Shapiro, N. M., Margerin, L., Campillo, M., van Tiggelen, B. A., & Weaver, R. L. (2001). Observation of equipartition of seismic waves. *Physical Review Letters*, *86*(15), 3447–3450. https://doi.org/10.1103/PhysRevLett.86.3447

Hughes, D. S., & Kelly, J. L. (1953). Second-order elastic deformation of solids. *Physics Review*, *92*(5), 1145–1149. https://doi.org/10.1103/PhysRev.92.1145

Komatitsch, D., & Tromp, J. (2003). A perfectly matched layer absorbing boundary condition for the second-order seismic wave equation. *Geophysical Journal International*, *154*(1), 146–153. https://doi.org/10.1046/j.1365-246X.2003.01950.x

Komatitsch, D., & Vilotte, J.-P. (1998). The spectral element method: An efficient tool to simulate the seismic response of 2D and 3D geological structures. *Bulletin of the Seismological Society of America*, *88*, 368–392.

Larose, E., Planès, T., Rossetto, V., & Margerin, L. (2010). Locating a small change in a multiple scattering environment. *Applied Physics Letters*, *96*(20), 204101. https://doi.org/10.1063/1.3431269

Lehujeur, M., Vergne, J., Maggi, A., & Schmittbuhl, J. (2017). Ambient noise tomography with non-uniform noise sources and low aperture networks: Case study of deep geothermal reservoirs in northern Alsace, France. *Geophysical Journal International*, *208*(1), 193–210. https://doi.org/10.1093/gji/ggw373

Lehujeur, M., Vergne, J., Schmittbuhl, J., & Maggi, A. (2014). Investigating a deep geothermal reservoir using ambient noise correlation, in: EGU General Assembly Conference Abstracts. (pp. 13,798).

Lin, F.-C., Li, D., Clayton, R. W., & Hollis, D. (2013). High-resolution 3D shallow crustal structure in Long Beach, California: Application of ambient noise tomography on a dense seismic array. *Geophysics*, *78*(4), Q45–Q56. https://doi.org/10.1190/geo2012-0453.1

Lockner, D. A., Walsh, J. B., & Byerlee, J. D. (1977). Changes in seismic velocity and attenuation during deformation of granite. *Journal of Geophysical Research*, *82*(33), 5374–5378. https://doi.org/10.1029/JB082i033p05374

Mainsant, G., Larose, E., Brönnimann, C., Jongmans, D., Michoud, C., & Jaboyedoff, M. (2012). Ambient seismic noise monitoring of a clay landslide: Toward failure prediction. *Journal of Geophysical Research*, *117*, F01030. https://doi.org/10.1029/2011JF002159

Margerin, L., Campillo, M., Shapiro, N. M., & van Tiggelen, B. (1999). Residence time of diffuse waves in the crust as a physical interpretation of coda *Q*: Application to seismograms recorded in Mexico. *Geophysical Journal International*, *138*(2), 343–352. https://doi.org/10.1046/j.1365-246X.1999.00897.x

Margerin, L., Campillo, M., & Van Tiggelen, B. (2000). Monte Carlo simulation of multiple scattering of elastic waves. *Journal of Geophysical Research*, *105*(B4), 7873–7892. https://doi.org/10.1029/1999JB900359

Margerin, L., Planès, T., Mayor, J., & Calvet, M. (2016). Sensitivity kernels for coda-wave interferometry and scattering tomography: Theory and numerical evaluation in two-dimensional anisotropically scattering media. *Geophysical Journal International*, *204*(1), 650–666. https://doi.org/10.1093/gji/ggv470

Michaels, J. E., & Michaels, T. E. (2005). Detection of structural damage from the local temporal coherence of diffuse ultrasonic signals. *IEEE Transactions on Ultrasonics, Ferroelectrics, and Frequency Control*, *52*(10), 1769–1782. https://doi.org/10.1109/TUFFC.2005.1561631

Moschetti, M. P., Ritzwoller, M. H., & Shapiro, N. M. (2007). Surface wave tomography of the western United States from ambient seismic noise: Rayleigh wave group velocity maps. *Geochemistry, Geophysics, Geosystems*, *8*, Q08010. https://doi.org/10.1029/2007GC001655

Nakamura, Y. (1977). Seismic energy transmission in an intensively scattering environment. *Journal of Geophysics Zeitschrift Geophysik*, *43*, 389–399.

Obermann, A., Froment, B., Campillo, M., Larose, E., Planes, T., Valette, B., et al. (2014). Seismic noise correlations to image structural and mechanical changes associated with the M_w 7.9 2008 Wenchuan earthquake. *Journal of Geophysical Research: Solid Earth*, *119*, 3155–3168. https://doi.org/10.1002/2013JB010932

Obermann, A., Planès, T., Larose, E., Sens-Schönfelder, C., & Campillo, M. (2013). Depth sensitivity of seismic coda waves to velocity perturbations in an elastic heterogeneous medium. *Geophysical Journal International*, *194*(1), 372–382. https://doi.org/10.1093/gji/ggt043

Olivier, G., Brenguier, F., Campillo, M., Lynch, R., & Roux, P. (2015). Body-wave reconstruction from ambient seismic noise correlations in an underground mine. *Geophysics*, *80*(3), KS11–KS25. https://doi.org/10.1190/geo2014-0299.1

Planès, T., & Larose, E. (2013). A review of ultrasonic coda wave interferometry in concrete. *Cement and Concrete Research*, *53*, 248–255. https://doi.org/10.1016/j.cemconres.2013.07.009

Poupinet, G., Ellsworth, W. L., & Frechet, J. (1984). Monitoring velocity variations in the crust using earthquake doublets: An application to the Calaveras fault, California. *Journal of Geophysical Research*, *89*(B7), 5719–5731. https://doi.org/10.1029/JB089iB07p05719

Remacle, J.-F., Lambrechts, J., Seny, B., Marchandise, E., Johnen, A., & Geuzainet, C. (2012). Blossom-Quad: A non-uniform quadrilateral mesh generator using a minimum-cost perfect-matching algorithm. *International Journal for Numerical Methods in Engineering*, *89*(9), 1102–1119. https://doi.org/10.1002/nme.3279

Rossetto, V., Margerin, L., Planès, T., & Larose, E. (2011). Locating a weak change using diffuse waves: Theoretical approach and inversion procedure. *Journal of Applied Physics*, *109*(3), 034903. https://doi.org/10.1063/1.3544503

Roux, P., Sabra, K. G., Gerstoft, P., Kuperman, W. A., & Fehler, M. C. (2005). *P*-waves from cross-correlation of seismic noise. *Geophysical Research Letters*, *32*, L19303. https://doi.org/10.1029/2005GL023803

Rummel, F. (1992). Physical properties of the rock in the ganitic section of borehole GPK1, Soultz-Sous-Forêt. Geotherm. Energy Eur. Soultz Hot Dry Rock Proj. 3.

Ryzhik, L., Papanicolaou, G., & Keller, J. B. (1996). Transport equations for elastic and other waves in random media. *Wave Motion*, *24*(4), 327–370. https://doi.org/10.1016/S0165-2125(96)00021-2

Sens-Schönfelder, C., & Wegler, U. (2006). Passive image interferometry and seasonal variations of seismic velocities at Merapi Volcano, Indonesia. *Geophysical Research Letters*, *33*, L21302. https://doi.org/10.1029/2006GL027797

Shapiro, N. M., Campillo, M., Margerin, L., Singh, S. K., Kostoglodov, V., & Pacheco, J. (2000). The energy partitioning and the diffusive character of the seismic coda. *Bulletin of the Seismological Society of America*, *90*, 655–665.

Shapiro, N. M., Campillo, M., Stehly, L., & Ritzwoller, M. H. (2005). High resolution surface wave tomography from ambient seismic noise. *Science*, *307*, 1615–1618.

Shapiro, N. M., & Campillo, M. (2004). Emergence of broadband Rayleigh waves from correlations of the ambient seismic noise. *Geophysical Research Letters*, *31*, L07614. https://doi.org/10.1029/2004GL019491

Shokouhi, P., Zoëga, A., Wiggenhauser, H., & Fischer, G. (2012). Surface wave velocity-stress relationship in uniaxially loaded concrete. *A C I Materials Journal*, *109*(2), 141–148.

Sneddon, I. N., & Murnaghan, F. D. (1954). Finite deformation of an elastic solid. *The Mathematical Gazette*, *38*(326), 305. https://doi.org/10.2307/3611182

Snieder, R. (2002). Coda wave interferometry for estimating nonlinear behavior in seismic velocity. *Science*, *295*(5563), 2253–2255. https://doi.org/10.1126/science.1070015

Snieder, R. (2006). The theory of coda wave interferometry. *Pure and Applied Geophysics*, *163*(2-3), 455–473. https://doi.org/10.1007/s00024-005-0026-6

Stacey, R. (1988). Improved transparent boundary formulations for the elastic-wave equation. *Bulletin of the Seismological Society of America*, *78*, 2089–2097.

Stehly, L., Campillo, M., & Shapiro, N. M. (2007). Traveltime measurements from noise correlation: Stability and detection of instrumental time-shifts. *Geophysical Journal International*, *171*(1), 223–230. https://doi.org/10.1111/j.1365-246X.2007.03492.x

Weaver, R. L. (1982). On diffuse waves in solid media. *The Journal of the Acoustical Society of America*, *71*(6), 1608–1609. https://doi.org/10.1121/1.387816

Weaver, R. L. (1990). Diffusivity of ultrasound in polycrystals. *Journal of the Mechanics and Physics of Solids*, *38*(1), 55–86. https://doi.org/10.1016/0022-5096(90)90021-U

Weaver, R. L., Hadziioannou, C., Larose, E., & Campillo, M. (2011). On the precision of noise correlation interferometry: Precision of noise correlation interferometry. *Geophysical Journal International*, *185*(3), 1384–1392. https://doi.org/10.1111/j.1365-246X.2011.05015.x

Wegler, U., & Lühr, B. G. (2001). Scattering behaviour at Merapi Volcano (Java) revealed from an active seismic experiment. *Geophysical Journal International*, *145*(3), 579–592. https://doi.org/10.1046/j.1365-246x.2001.01390.x

Wu, R.-S. (1985). Multiple scattering and energy transfer of seismic waves—Separation of scattering effect from intrinsic attenuation—I. Theoretical modelling. *Geophysical Journal International*, *82*(1), 57–80. https://doi.org/10.1111/j.1365-246X.1985.tb05128.x

Yamamura, K., Sano, O., Utada, H., Takei, Y., Nakao, S., & Fukao, Y. (2003). Long-term observation of in situ seismic velocity and attenuation. *Journal of Geophysical Research*, *108*(B6), 2317. https://doi.org/10.1029/2002JB002005

Zigone, D., Ben-Zion, Y., Campillo, M., & Roux, P. (2015). Seismic tomography of the Southern California plate boundary region from noise-based Rayleigh and Love waves. *Pure and Applied Geophysics*, *172*(5), 1007–1032. https://doi.org/10.1007/s00024-014-0872-1